Available online at www.sciencedirect.com
ScienceDirect
Trans. Nonferrous Met. Soc. China 34(2024) 2231−2244
Transactions of Nonferrous Metals Society of China
www.tnmsc.cn

# Achieving high strength and antibacterial Zn−4Ag−Mn alloy with homogenous corrosion behavior via high-pressure solid solution

Kun-ning NIU[1], De-chuang ZHANG[2], Fu-gang QI[1], Jian-guo LIN[2], Yi-long DAI[1]

1. School of Materials Science and Engineering, Xiangtan University, Xiangtan 411105, China;
2. Key laboratory of Low Dimensional Materials and Application Technology of Ministry of Education, Xiangtan University, Xiangtan 411105, China

Received 11 January 2023; accepted 26 September 2023

**Abstract:** Zn−4Ag−Mn alloy was successfully prepared by high-pressure solid solution (HPS) method to achieve high strength and antibacterial implant materials which can degrade uniformly. Microstructural characterization showed that HPS treatment on Zn−4Ag−Mn alloy resulted in 57.9% grain refinement, and the average size of the second phases was reduced to 10.2 μm compared with as-cast (AC) alloy. The compression, Vickers hardness and wear and friction tests showed particularly high mechanical properties of HPS alloys, including a compressive yield strength of 333.5 MPa and a Vickers hardness of Hv 89.5. Electrochemical corrosion, and immersion corrosion tests showed that HPS treatment optimized the corrosion resistance of the alloy with homogenous corrosion. Furthermore. The HPS-treated Zn−4Ag−Mn alloy exhibited excellent antibacterial properties through antibacterial testing, with an antibacterial rate of 71.6%. These results suggest that the HPS-treated Zn−4Ag−Mn alloy can be considered as a promising biodegradable implant material.

**Key words:** Zn−Ag−Mn alloy; high-pressure solid solution; high strength; homogenous corrosion; antibacterial property

## 1 Introduction

The recent rapid developments of medical implant materials have played an important role in the treatment of diseases, such as fractures and blood clotting [1]. Traditional permanent implants (stainless steel, titanium, cobalt-based alloys, etc.) usually need to be removed after recovering [2]. Biodegradable metallic implants offer significant advantages in this regard, as they can be removed without secondary surgery, reducing physical pain and financial strain for the patients. Therefore, the biodegradable metals (BMs) are potential alternatives to permanent implants and are regarded as the next generation of revolutionary metallic biomaterials [3,4].

Corrosion rate is the main factor to classify biodegradable metals. Magnesium (Mg), zinc (Zn) and iron (Fe) alloys as potential alloys for BMs have been intensively studied. The rapid corrosion of magnesium is associated with the accumulation of corrosion products and the release of large amounts of hydrogen, which may lead to a sudden loss of mechanical support, hindering the clinical application of magnesium-based alloys [5]. In contrast, Fe-based alloys exhibit relatively slow degradation rate and excellent mechanical properties, but superior corrosion resistance [6] may prevent newly formed tissue from making desired replacements [7]. In recent years, zinc has become a competitor to magnesium and iron, with a degradation rate between the two metals [8]. However, pure Zn is limited in clinical application

**Corresponding author:** Jian-guo LIN, Tel: +86-15080788918, E-mail: lin_j_g@xtu.edu.cn;
Yi-long DAI; Tel: +86-731-58298408; E-mail: daiyilong@xtu.edu.cn
DOI: 10.1016/S1003-6326(24)66537-4

due to its low strength and local corrosion. Alloying is a common and effective way to overcome the limitations of mechanical and corrosion properties of Zn. In BMs, the biocompatibility of alloying elements must be carefully considered. Therefore, silver (Ag) has been suggested as an alloying element in zinc-based alloys because of its ability to improve mechanical properties while maintaining biocompatibility. Ag containing materials are widely used in dental implants [9]. In addition to this, many studies have been initiated based on the antimicrobial properties of Ag, and it has been demonstrated that Ag ions or Ag nanoparticles can kill bacteria and prevent them from adhering to the surface of implants [10]. Previous studies have confirmed the excellent mechanical properties, predictable degradation behavior, acceptable biocompatibility and effective antibacterial properties of Zn−4Ag, making it a candidate of biodegradable materials [11]. On this basis, the addition of a third component was considered to further optimize its properties, and it was shown that the addition of manganese (Mn) to Zn significantly improved its elongation (>70% elongation) [12] and biocompatibility [13].

In recent years, high-pressure technology has been widely studied and applied as a means of improving mechanical properties of Mg alloys [14]. The high-pressure process can not only effectively reduce the grain size of the alloy, but also obtain a non-equilibrium solidification microstructure that is difficult to obtain under atmospheric pressure [15]. The present study found that high pressure solution treatment can improve the solid solubility and mechanical strength of Li in binary Zn−Li alloy [16,17], but its effect on ternary Zn alloy is still unknown. Whether high pressure solution treatment can improve the solubility of alloying elements in Zn or only one element is unclear. In this study, to further optimize the microstructure and properties of Zn−4Ag−Mn, Zn−4Ag−Mn alloys were treated by high pressure solid solution method. The microstructure, mechanical properties, corrosion, frictional wear and antibacterial properties of Zn−4Ag−Mn alloys were investigated.

## 2 Experimental

### 2.1 Materials preparation

The Zn−4wt.%Ag−1wt.%Mn (denoted as Zn−4Ag−Mn) was prepared by conventional casting method using pure Zn (purity of 99.99%), pure Ag (purity of 99.99%), and Mg−Mn master alloy. The melting process was carried out in a furnace under argon atmosphere to obtain as-cast sample (AC). To homogenize the ingots, they were annealed at 300 °C for 10 h and then quenched. Cylindrical samples with a height of 20 mm and a diameter of 10 mm were cut from the ingot and ground for high-pressure solid solution (HPS). HPS treatment was carried out using a high pressure six-sided top device (CS−1B, Zhengzhou Abrasive Grinding Institute Co., Ltd., China) to heat the cylinders to 450 °C for 1 h under a pressure of 3 GPa, followed by rapid cooling to room temperature. The actual chemical compositions of the metal ingots were determined by X-ray fluorescence (XRF; S4 Pioneer, Bruker, Germany) and the results are given in Table 1.

**Table 1** Chemical compositions of Zn−4Ag−Mn alloys (wt.%)

| Alloy | Ag | Mn | Zn |
|---|---|---|---|
| AC Zn−4Ag−Mn | 4.05±0.06 | 1.02±0.05 | Bal. |
| HPS-treated Zn−4Ag−Mn | 4.09±0.15 | 1.04±0.09 | Bal. |

### 2.2 Microstructure characterization

Polarized light microscope and scanning electron microscopy (SEM, MIRA3, LMH, Oxford, UK) and energy dispersive spectroscopy (EDS, X-Max20, Oxford, UK) were used to examine the microstructure and composition of the samples at 15 kV. All samples were polished before observation and etched with nitric acid alcohol with a volume fraction ratio of 0.5:99.5. The phase compositions of the samples and corrosion products were analyzed by Cu $K_\alpha$ radiation ($\lambda$=1.5406 nm) and scanned at a rate of 4 (°)/min in the $2\theta$ range of 10°−90° by X-ray diffraction (XRD, U1tima IV, Tokyo, Japan).

### 2.3 Mechanical tests

The Vickers hardness test of the specimen was carried out on ZHVST−30F micro Vickers hardness tester with the applied load of 2 kg and holding time of 10 s. The test was performed 5 times, and the average value was taken as Vickers hardness. The compressive property of the specimens was tested by universal testing machine (Instron 3369, Boston, MA, USA) at a compression rate of

1 mm/min at room temperature. Three samples were used for each test and the result was the average of the three samples.

### 2.4 Electrochemical tests

The electrochemical corrosion behavior of the samples was evaluated by using an electrochemical workstation (Par Stat 2273, Princeton Applied Research Institute, USA) in Hanks' solution at 37 °C, including potentiodynamic polarization and electrochemical impedance spectroscopy (EIS). The sample with an exposed area of 0.785 $cm^2$ was used as the working electrode, the platinum sheet was used as the counter electrode, and the saturated glycerol electrode (SCE) was used as the reference electrode. The EIS test was preceded by an open-circuit potential (OCP) test to determine the stability of the open-circuit voltage. The frequency of EIS test ranged from 0.01 Hz to 100 kHz with a disturbance signal amplitude of 10 mV. Potential dynamic polarization tests were performed with a scanning rate of 1 mV/s from the cathodic potential −0.5 V (vs OCP) to the anodic potential + 0.5 V (vs OCP). Finally, the corrosion rate of the sample was calculated according to ASTM G102—89 [18]:

$$R_c=K\cdot J_{corr}\cdot W/\rho \quad (1)$$

where $R_c$ is the corrosion rate (mm/a), $K$ is a constant taken as $3.27\times10^{-3}$ mm·g/(μA·cm·a), $J_{corr}$ is the corrosion current density (μA/$cm^2$), $\rho$ is the density of the metal (g/$cm^3$), and $W$ is the equivalent mass of Zn (taken as 32.68).

### 2.5 Immersion tests

The immersion test was performed at 37 °C in Hanks' solution for 30 d and three parallel samples were used for each test. The ratio of immersing solution volume to surface area was set as 20:1 mL/$cm^2$ [19]. In order to analyze the corrosion products, the samples were taken out to observe the corrosion morphology after immersion by SEM. The chemical composition of the corrosion products was identified by EDS. The functional groups of the corrosion products were confirmed by Fourier infrared analysis (FTIR, Nicolet 6700) recorded from 4000 to 500 $cm^{-1}$.

### 2.6 Friction and wear test

The friction and wear behaviors were investigated using high-speed reciprocating friction tester (HSR−2M; Zhongke Kaihua Technology Development Co., Ltd., Lanzhou, China) with a load of 2 N, a stroke length of 5 mm, a frequency of 1 Hz, and a test time of 15 min. By measuring the mass of the sample before and after the friction wear test, the mass loss of the samples was determined by using an electronic balance.

### 2.7 Antibacterial effect evaluation

*E. coli* was extracted using a disposable sterile inoculation loop and inoculated in 500 mL of phosphate buffer solution (PBS) buffer cooled to 37 °C to prepare a bacterial suspension. The bacterial suspensions were incubated in a constant temperature and humidity chamber at 37.5 °C for 24 h. The experimental samples ($d$10 mm × 1 mm) were autoclaved in an autoclave at 120 °C for 30 min. The experimental samples were placed in 24-well plates. 1 mL of *E. coli* suspension was dropped onto the sample surface with a sterile dropper, and the same suspension was also dropped into the no-sample control group. After that, the 24-well culture plates were incubated in a constant temperature incubator for 24 h. After the incubation was completed, 0.1 mL of bacterial suspension from each well was dropped onto a different agar plate and incubated in a constant temperature incubator for 24 h. After the final incubation, the surface medium was counted and the antibacterial rate was calculated according to [20]

$$R_a=\frac{N_c-N_e}{N_c}\times100\% \quad (2)$$

where $R_a$ represents the antibacterial rate, $N_c$ is the number of colonies in the control group and $N_e$ is the number of colonies in the experimental medium.

### 2.8 Statistical methods

All quoted errors and error bars correspond to sample standard errors.

## 3 Results and discussion

### 3.1 Microstructure and mechanical properties

Figure 1 shows the XRD patterns of AC and HPS alloys. It can be seen that the AC and HPS samples were mainly composed of Zn matrix, $AgZn_3$ phase and $MnZn_{13}$ phase, which was consistent with previous studies [12,21−24]. The intensity of the diffraction peaks of Zn phase after

high-pressure solid solution was significantly enhanced and that of the $AgZn_3$ phase was significantly weakened. The diffraction peak of $MnZn_{13}$ phase became stronger, indicating that more $MnZn_{13}$ phase was precipitated after HPS treatment.

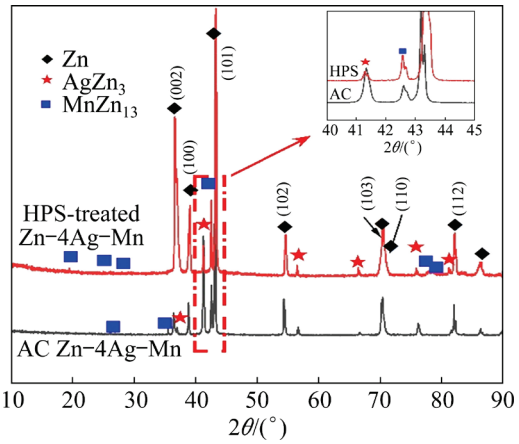


**Fig. 1** XRD patterns of as-cast (AC) and high-pressure solid solution (HPS)-treated Zn−4Ag−Mn alloys

Figure 2 shows the polarized optical microstructure images and grain distribution diagram of AC and HPS-treated samples. The grain histograms were measured by Nano Measurer, where $\mu_g$ represents the average value, and $d_{90}$ and $d_{25}$ represent grain sizes below 90% and below 25%, respectively. From Fig. 2, it can be seen that 90% of the grain size in AC alloy was below 433.40 μm and 25% of the grain size was below 235.76 μm, while 90% of the grain size of HPS alloy was below 197.55 μm and 25% of the grain size was below 80.29 μm. The result showed that the average grain size of HPS alloy was reduced from 336.54 to 141.67 μm after high pressure solid solution, which reached grain refinement by 57.9%.

Figure 3 shows the SEM images of AC and HPS-treated samples, the results of EDS analysis of different regions, and the percentage and size of the second phase derived from the SEM processed by Image-Pro-Plus 6.0. From Figs. 3(a, b), white dendrites were found in AC and HPS-treated samples, which were confirmed as $AgZn_3$ and $MnZn_{13}$ phases by the results of EDS and XRD, while gray region was the Zn matrix phase [25]. The second phases of AC alloy were coarse and massive, while the size of the second phases in HPS-treated alloy was significantly reduced with the distribution of dotted and thin stripes. The decrease in Ag content and increase in Mn content at Point 3 compared to Point 2 from EDS analysis also indicated that more Ag atoms solubilized into the Zn matrix, and $MnZn_{13}$ was precipitated from Zn matrix, which corresponded to the XRD results in Fig. 1. As shown in Fig. 3(d), the area fraction of

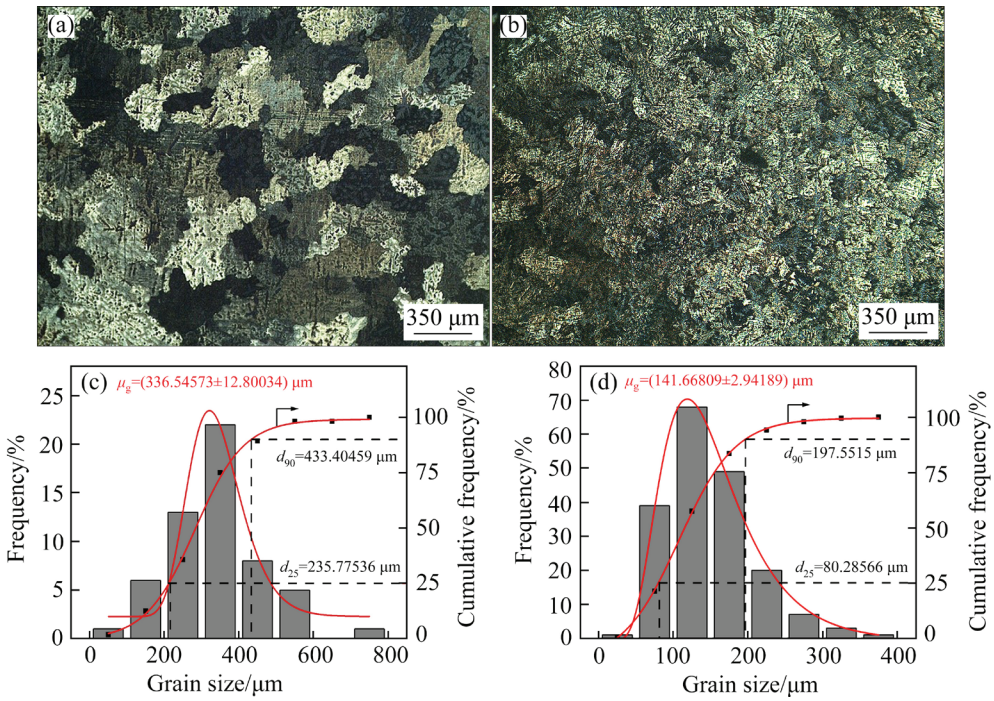


**Fig. 2** OM images (a, b) and grain size distributions (c, d) of alloys: (a, c) AC Zn−4Ag−Mn; (b, d) HPS-treated Zn−4Ag−Mn

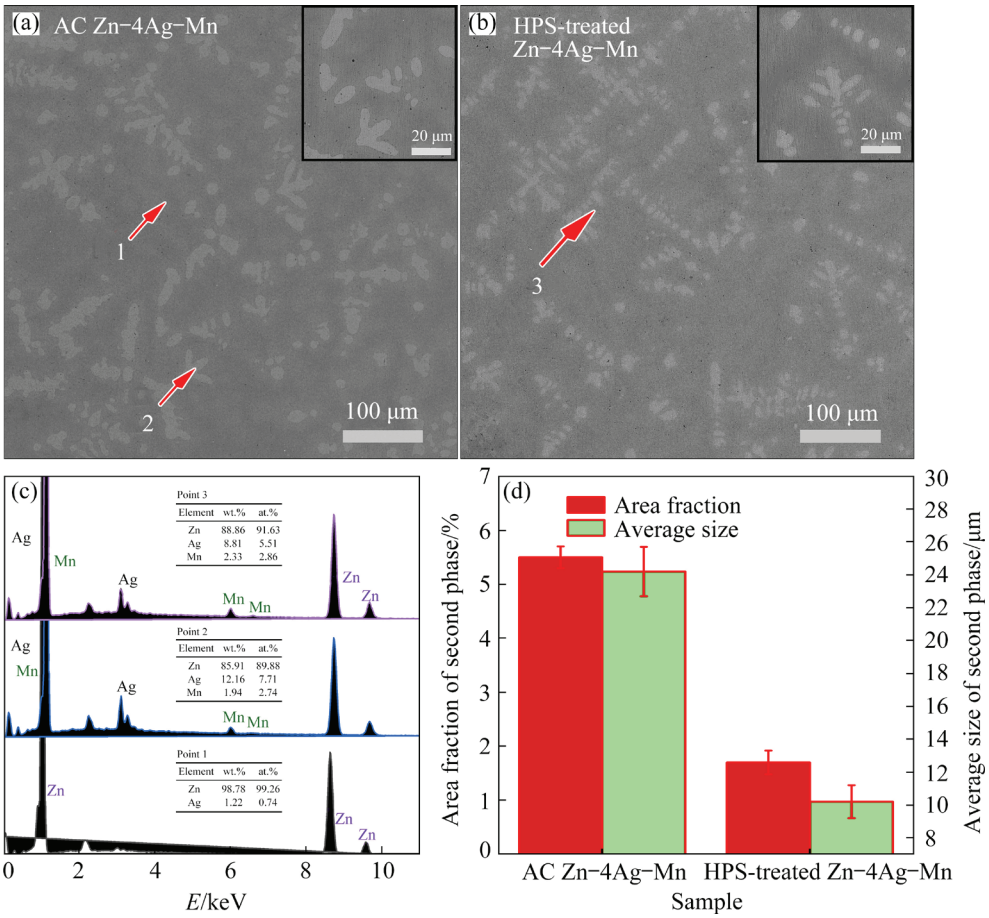


**Fig. 3** SEM analysis results of AC and HPS-treated Zn−4Ag−Mn alloys: (a, b) SEM images; (c) EDS results; (d) Histogram of area fraction and average size of second phases

the second phases in AC alloy was 5.5% and the average size of second phases was 24.2 μm, while the area fraction of the second phase after high-pressure solid solution in HPS-treated alloy was reduced to 1.7% and the average size was reduced to be 10.2 μm. Thus, the high-pressure solid solution not only solubilized part of Ag atoms into Zn phase but also refined the size of the second phases to make them more uniform and diffusive.

LI et al [16] reported that HPS treatment could greatly promote the capacity of solid solution in Zn–*x*Li binary alloys and expand the solid dissolution zone, which is attributed to the fact that ultrahigh pressure weakens the binding force between iso-atoms but enhances that of the hetero-atoms. According to the experimental results of this study, the effect of HPS treatment on the solid solubility of Zn–Li binary alloy and Zn−Ag−Mn ternary alloy is different. High pressure solution treatment did not improve the solid solubility of both Ag and Mn atoms in Zn matrix, but only improved the solid solubility of Ag atoms in Zn.

It is reported that efficiency of forming Zn−X intermetallic compounds is defined with a decreasing rank as follows: Mn > Li > Ag > Cu > Mg [26]; therefore, Mn and Zn are more likely to form Zn−X intermetallic compounds. In addition, the content of Ag is 4 times than that of Mn, and the maximum solid solubility of Ag atoms in Zn (5 at.% at 431 °C) is greater than that of Mn atoms (0.6 at.% at 417.25 °C) at atmospheric pressure. Therefore, after high pressure solid solution, more Ag atoms are dissolved into the interstitial space of Zn phase in comparison. Due to the limited space in the Zn lattice, a small amount of Mn atoms in the original solid solution in the Zn phase would precipitate to form $MnZn_{13}$ phases.

The specific mechanisms are summarized as:

(1) Firstly, $AgZn_3$ is a coarse phase in AC alloy while $MnZn_{13}$ is a fine phase in HPS-treated alloy. After high pressure solid solution, part of $AgZn_3$ phases dissolved into the Zn matrix, while fine and diffused $MnZn_{13}$ precipitated.

(2) The formula for crystal growth is [27]

$$U=\frac{fD}{a}\left[1-\exp\left(-\frac{\Delta G}{RT}\right)\right] \quad (3)$$

where $U$ is the crystal growth rate, $a$ is the atomic spacing, $D$ is the diffusion coefficient, $f$ is a factor related to the interfacial condition, indicating the proportion of positions at the interface suitable for growth in the whole interface, and $\Delta G$ is the free energy difference between the liquid and solid phases. The increasing pressure leads to the reduction of atomic spacing and the dominant role of atomic diffusion, so the growth of grain is inhibited. The pressure inhibits the growth of grains, so the grain size of Zn−4Ag−Mn is reduced at high pressure, causing the materials to be uniform and diffusive.

(3) During the process of HPS, the recrystallization of Zn alloys occurs and the grains re-nucleate. In crystallography, the nucleation rate of a material can be expressed as [28]:

$$I=I_0\exp\left(-\frac{\lambda\Delta S_m}{R\tau^2(1-\tau)^3}\right)\cdot \exp\left(-\frac{E_0+1/3PV_0}{RT}\right)=I_0\exp(-G) \quad (4)$$

where $I_0$ and $\lambda$ are constants, $\Delta S_m(=\Delta H_m/T_m)$, $\Delta H_m$ is the latent heat of melting, $\tau$ is the relative subcooling, $E_0$ is the activation energy of crystallization at atmospheric pressure, $P$ is the pressure, $V_0$ is the atomic volume, and $G$ is the nucleation activation energy. Obviously, the smaller the $G$, the larger the nucleation rate. The partial derivative of $P$ gives

$$\left(\frac{\partial G}{\partial P}\right)_T=\Delta G\left(5-\frac{2}{\tau}\right)\frac{1}{T_m}\frac{dT_m}{dP}+\Delta G\frac{1}{\Delta S_m}\Delta G\frac{d\Delta S_m}{dP}+\frac{1}{3}V_0 \quad (5)$$

Compared with the first two terms, the last term has a smaller quantity and can be neglected; therefore, the above equation is determined by the first two terms. With increasing the pressure from high-pressure solid solution, the nucleation rate increases rapidly and the number of grains increases.

Figure 4 shows the mechanical properties of the AC and HPS-treated alloys including the compressive yield strength (CYS) and Vickers hardness. From the engineering stress−strain curves in Fig. 4(a), it can be seen that the compressive yield strength of the HPS-treated alloy was significantly higher than that of AC alloy. The CYS of HPS-treated alloy increased from 218.7 to 333.5 MPa with an increase of 52.5%, while the Vickers hardness of HPS-treated alloy increased from Hv 72.5 to Hv 89.5. Therefore, the mechanical properties of Zn−4Ag−Mn alloy were significantly improved after high-pressure solid solution.

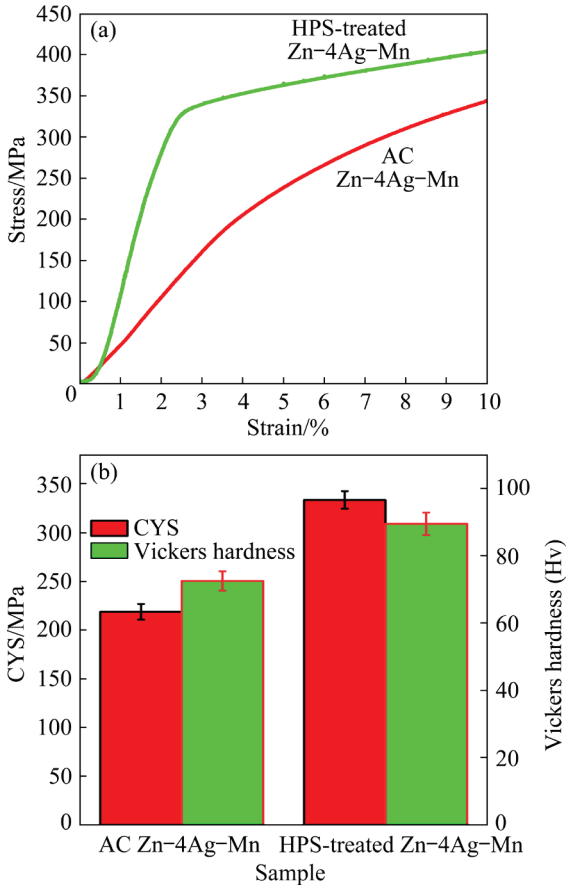


**Fig. 4** Mechanical properties of AC and HPS-treated alloys: (a) Engineering stress−strain curve; (b) Compressive yield strength (CYS) and Vickers hardness histogram

Based on the aforementioned characterization, the improvement in yield strength ($\sigma_{YS}$) of HPS-treated Zn−4Ag−Mn samples can be principally attributed to grain boundary strengthening ($\sigma_{GB}$), solid solution strengthening ($\sigma_{SS}$) and precipitation hardening ($\sigma_P$):

(1) Grain refinement

The combination of high pressure and water cooling leads to lattice distortion and a large

number of dislocations inside the grain, which reduces the nucleation activation energy and increases the nucleation rate, resulting in grain refinement. According to the Hall−Patch law, a fine grain can enhance the mechanical properties of alloys:

$$\sigma_{GB}=\sigma_0+Kd^{-1/2} \quad (6)$$

where $\sigma_0$ and $K$ are constants related to be material. As the grain size ($d$) of HPS-treated alloy was reduced from 336.54 μm (AC alloy) to 141.67 μm, high-pressure solid solution acts as a fine grain reinforcement.

(2) Solid solution strengthening

Effect of solid solution strengthening on the strength increment can be expressed by Fleischer equation:

$$\sigma_{ss}=\sigma_0'+Z_F G'(|\delta|+\beta|\eta|)^{3/2}C^{1/2} \quad (7)$$

where $\sigma_0'$ is the yield strength of a pure metal, $Z_F$ is a constant, $\beta$ is between 1/20 and 1/16, $C$ is the alloying content (at.%), $G'$ is the shear modulus of the metal, and $\delta$ and $\eta$ are the degree of the atomic size mismatch and the modulus mismatch between the solute atom and solvent atoms, respectively. After HPS treatment, more Ag atoms are dissolved into the lattice of Zn, which plays the role of solid solution strengthening. Although the precipitation of Mn can definitely weaken the solid solution strengthening effect, the amount of Ag atoms in solution is much larger than that of Mn atoms of precipitation, and the total solid solution strengthening effect is increased.

(3) Precipitation hardening

The HPS treatment increases the solid solubility of Ag in Zn, and more Ag atoms are dissolved into the interstitial space of the Zn phase. Due to the limited space in the Zn lattice, a small amount of Mn atoms in the original solid solution precipitate to form fine $MnZn_{13}$ phases. In addition, after HPS treatment, the second phase in the AC alloy is broken and its size is reduced. The fine precipitates can inhibit the movement of dislocations, and the dislocations bypass or shear through the second phases to improve the strength of the material [29]. According to the Orowan formula, the shear stress ($\sigma_P$) is proportional inversely to the spacing of second phases ($\lambda_s$):

$$\sigma_P=G'b/\lambda_s \quad (8)$$

where $b$ is the magnitude of Burger's vector. As the HPS-treated alloy possesses finer precipitates, stronger precipitation hardening effect is achieved.

### 3.2 Corrosion performance and corrosion mechanism

3.2.1 Electrochemical corrosion

Figure 5 shows the electrochemical corrosion properties of AC and HPS-treated alloys. From Fig. 5(a), AC and HPS-treated alloys exhibited a similar electrochemical corrosion process. An obvious passivation zone was found on anodic polarization curve, and electrochemical parameters of corrosion potential, corrosion current density, and corrosion rate were derived by fitting the Tafel curve in Table 2. The corrosion rate derived from the polarization curve to be 0.18 and 0.15 mm/a for AC and HPS-treated alloys, respectively. The HPS-treated sample showed a lower corrosion current density and corrosion rate with a positive corrosion potential than that of AC sample, indicating that HPS-treated alloy exhibited better corrosion resistance than AC alloy. According to Table 2, the corrosion rate of AC and HPS-treated Zn−4Ag−Mn alloy was higher than that of pure Zn. It is reported that the alloying of Ag elements could increase the corrosion rate of the alloy [30].

As shown in Fig. 5(b), impedance Nyquist diagram of both AC and HPS-treated alloys exhibited a capacitive arc, indicating that the same equivalent circuit was fitted. The equivalent circuit is composed of the resistance ($R$) and constant phase element (CPE). The solution resistance is denoted as $R_s$. The resistance and capacitance of the corrosion products on the specimen surface are denoted as $R_{ct}$ and $CPE_f$. In the low-frequency region, capacitive arc radius of HPS-treated alloy was significantly larger than that of AC alloy, which indicated that the charge was more difficult to transfer, and the greater the polarization resistance, the stronger the corrosion resistance in HPS-treated alloy. The pseudo-induction arc appeared in the low-frequency region, indicating that the corrosion products on the surface of AC sample in the later corrosion were easy to consume or fall off. From Fig. 5(c), the impedance mode value and phase angle of HPS-treated alloy were higher than those of AC alloy, which further confirmed more dense corrosion products formed on the surface of HPS-treated alloy than on AC alloy.

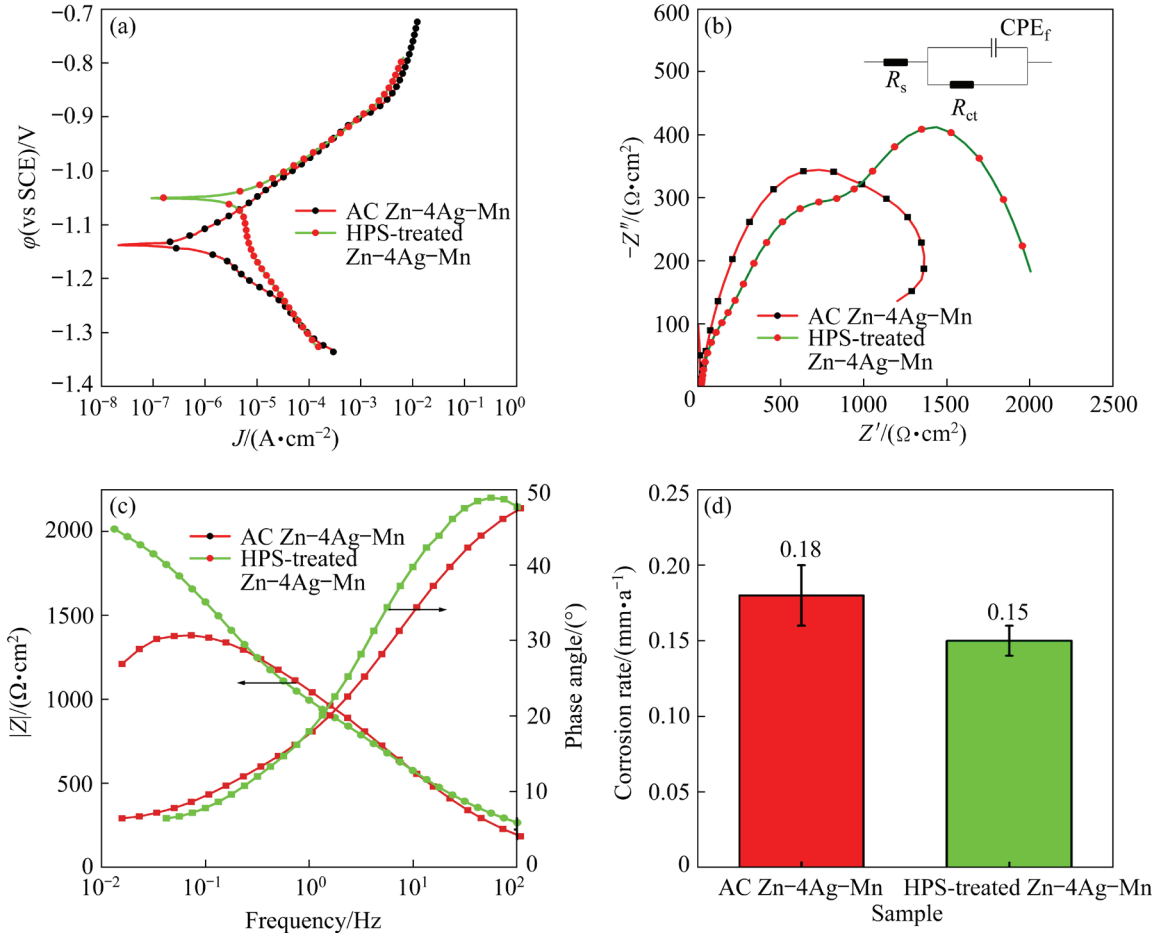


**Fig. 5** Electrochemical corrosion properties: (a) Polarization curves; (b) Nyquist plots and equivalent circuit; (c) Bode plots; (d) Corrosion rates

**Table 2** Electrochemical parameters and corrosion rates for Zn−4Ag−Mn alloys from polarization curves

| Sample | $\varphi_{corr}$(vs SCE)/V | $J_{corr}$/(μA·cm$^{-2}$) | $R_C$/(mm·a$^{-1}$) | Source |
|---|---|---|---|---|
| AC Zn−4Ag−Mn | −1.14±0.03 | 6.06±0.35 | 0.18±0.02 | This study |
| HPS-treated Zn−4Ag−Mn | −1.05±0.02 | 4.84±0.30 | 0.15±0.01 | This study |
| Pure Zn | −1.06 | 7.76 | 0.12 | Ref. [24] |

3.2.2 Immersion corrosion

The surface morphologies of AC and HPS-treated alloys immersed in Hanks' solution for 1 and 30 d were characterized (Fig. 6), and the corrosion products were analyzed by EDS (Table 3). After soaking for 1 d, a small amount of corrosion products were observed on the surface of the samples, and the volume fraction of corrosion products accumulated on the surface of AC samples was larger than that of HPS-treated samples. Moreover, the black corrosion products of HPS-treated samples accumulated in the position and the distribution of the second phases indicated that the corrosion started from the second phases. Therefore, the difference in the volume fraction of corrosion products on the surface of the two samples may be caused by the difference in the size and volume of the second phases.

After soaking for 30 d, the corrosion products on the surface of AC and HPS-treated samples were obviously stacked. The stacking of corrosion products on the surface of AC samples was uneven, while the stacking of corrosion products on the surface of HPS-treated samples was uniform. The difference in the morphology of the two corrosion products is mainly due to the potential difference

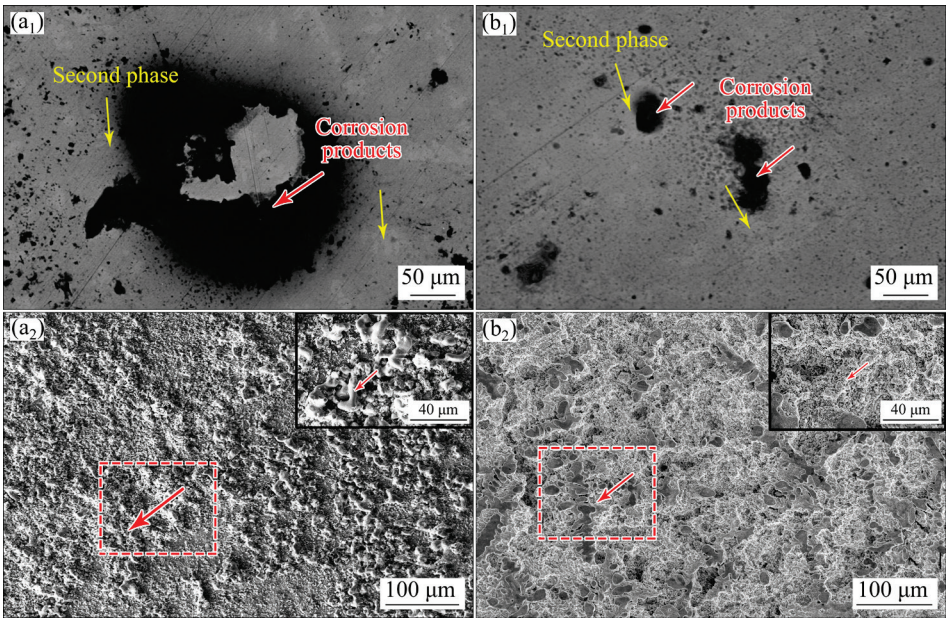


**Fig. 6** SEM images of AC ($a_1$, $b_1$) and HPS-treated ($a_2$, $b_2$) Zn−4Ag−Mn samples immersed in Hanks' solution: ($a_1$, $a_2$) Immersed for 1 d; ($b_1$, $b_2$) Immersed for 30 d

**Table 3** Chemical composition of corrosion products immersed in Hanks' solution for AC and HPS-treated Zn−4Ag−Mn alloys

| Alloy | Chemical composition/at.% | | | | | | | |
|---|---|---|---|---|---|---|---|---|
| | Zn | C | O | Na | P | Ca | Ag | Mn |
| AC Zn−4Ag−Mn | 16.41 | 14.72 | 50.16 | 7.49 | 5.28 | 2.39 | 0 .01 | 0.05 |
| HPS-treated Zn−4Ag−Mn | 19.99 | 15.12 | 50.20 | 10.32 | 2.05 | 0.64 | 0.02 | 0.03 |

between the Zn phase and the second phases, which leads to the corrosion of the micro-electric couple. The corrosion efficiency of the micro-electric couple represents the speed of the corrosion rate [31]. The volume fraction of the second phase in AC sample is large, and the distribution is uneven. Thus, the corrosion efficiency of the micro-electric couple is high, resulting in the formation of the local pitting corrosion. As the volume fraction of the second phases of HPS-treated samples is small and dispersed, the corrosion efficiency of its microcouples is low, resulting in slower and more homogenous corrosion.

The chemical composition of the corrosion products obtained from EDS analysis of the corresponding points in Fig. 6 is given in Table 3. In addition to Zn, Ag and Mn, the corrosion products of AC and HPS-treated alloys also contained C, O, Na, P and Ca. Na may be derived from Hanks' solution, where Zn alloys usually produce degradation products of calcium phosphate and calcium carbonate [31]. The high content of O indicates that the composition of corrosion products may be mainly oxides and insoluble hydroxides [32,33], which should be the results of the ionic reaction of $Zn^{2+}$ with several acid radicals such as $Cl^-$, $HCO_3^-$, and $HPO_4^{2-}$ in Hanks' solution [34].

The XRD patterns and FTIR spectra of the corrosion products after 30 d of immersion are shown in Fig. 7. The XRD patterns (Fig. 7(a)) show that the corrosion products of AC and HPS-treated were mainly ZnO, $Zn(OH)_2$ and $Zn_5(OH)_6(CO_3)_2$. The FTIR spectra of AC and HPS-treated alloys (Fig. 7(b)) show that a broad absorption at 2800−3323 $cm^{-1}$ was attributed to the hydroxyl of O—H stretching vibrations [35]. The absorption peaks around 1500, 1387−1580 $cm^{-1}$ for AC and HPS-treated alloys belonged to the antisymmetric $CO_3^{2-}$ ($\upsilon 3$) band, indicating the formation of carbonates in the samples [32]. The peaks observed in the wave number range of 830−890 $cm^{-1}$ belonged to the

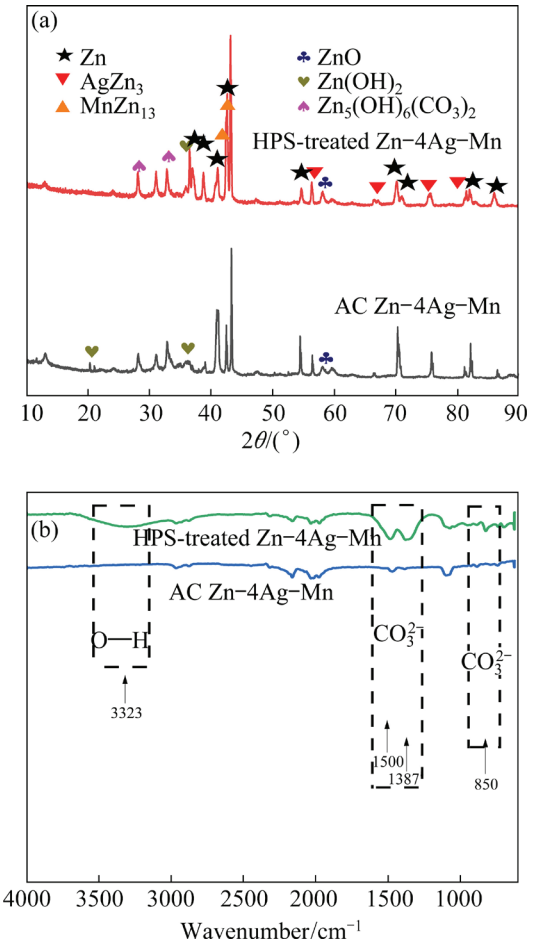


**Fig. 7** Analysis results of corrosion products of AC and HPS- treated alloys after 30 d of immersion in Hanks' solution: (a) XRD patterns; (b) FTIR spectra

$CO_3^{2-}$ ($\upsilon 2$) band [36]. The combined EDS, FTIR and XRD results of the corrosion products were confirmed as ZnO, $Zn(OH)_2$ and $Zn_5(OH)_6(CO_3)_2$.

Both electrochemical and immersion tests confirm that the corrosion resistance of HPS-treated alloy is better than that of AC counterpart. A large number of coarse second phases in the AC sample act as anode, and Zn matrix acts as the cathode. Thus, the formation of microcells accelerates the corrosion rate, while the second phases in HPS-treated alloys were broken and partly solid-solutionized into Zn matrix, with the fine uniform precipitation of $MnZn_{13}$ phases. Therefore, the areas of the anode in HPS alloy are reduced, decreasing the microcell effects and corrosion rate [15].

### 3.3 Friction and wear properties

As a bone implant, Zn alloy is rubbed with the bone in the process of service, so the friction and worn performance of the alloys are paid attention. Figure 8 shows the friction coefficient curve, friction coefficient and wear mass loss histogram of AC and HPS-treated alloys. AC and HPS-treated alloys showed similar frictional wear process, and the friction coefficient tended to be stable after 300 s of friction. The friction coefficient of HPS-treated alloy was lower than that of AC alloy, which indicated that HPS-treated alloy was more wear-resistant. Moreover, the wear loss of HPS-treated alloy was lower than that of AC alloy, which further confirmed the higher wear resistance of HPS-treated alloy. The friction wear performance is mainly affected by the microstructure and hardness. On the one hand, Vickers hardness of AC alloy was Hv 72.5, and that of HPS-treated alloy was Hv 89.5. On the other hand, the coarse second phases in AC sample possessed a decoupling effect on the Zn matrix phase, resulting in a lower wear resistance. In contrast, HPS-treated alloys had fine second phases dispersed in soft Zn matrix, thus minimizing the concentration of stress around the second phase particles and slowing down the Zn matrix unraveling.

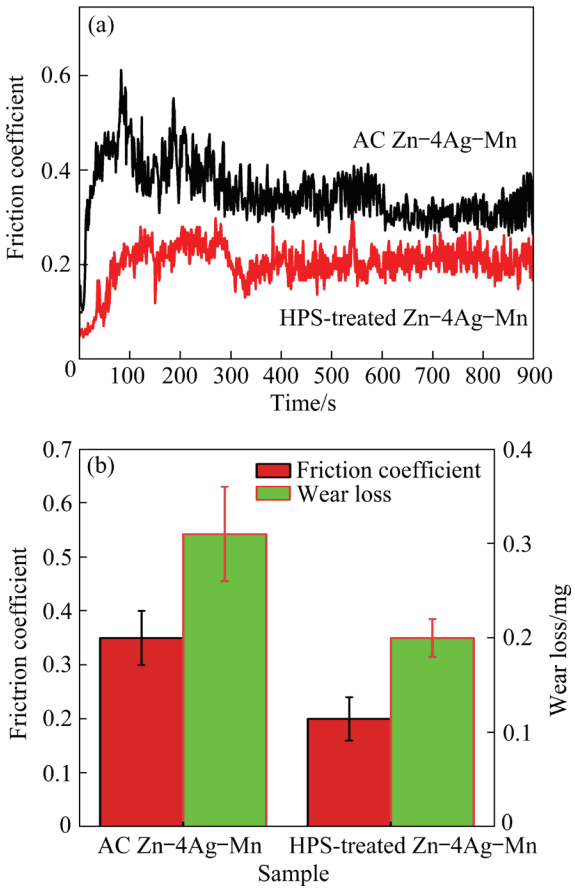


**Fig. 8** Friction and wear performance of AC and HPS-treated alloys: (a) Friction coefficient curve; (b) Friction coefficient and wear loss histogram

When a compressive load was applied during the friction wear test, uniformly distributed fine second phase particles protruded from the Zn matrix and played a strong role in load-bearing, reducing the wear of the Zn matrix and thus effectively improving the wear resistance of the HPS-treated alloy. Previous studies [15,37] confirmed that the fine distribution of hard particles in the matrix improve the wear resistance of the material, which results in HPS-treated alloy being more wear-resistant and having a more stable friction coefficient curve.

Figure 9 shows the SEM morphology and EDS result after the frictional wear testing in Hanks' solution. The deeper abrasion marks were found on the surface of AC sample than those on HPS-treated sample, which was related to the hardness and microstructure of the two materials. HPS sample showed high hardness and uniform microstructure, resulting in shallow and uniform wear marks. In the high magnification view of the morphology of AC sample, coarse grains act as a decomposition in the matrix resulting in poor wear resistance and higher wear loss in AC sample than in HPS-treated sample. The component of worn particles on the surface was determined by EDS, which consisted of a large amount of Zn and O elements, and it can be inferred that the wear debris was mainly ZnO [38].

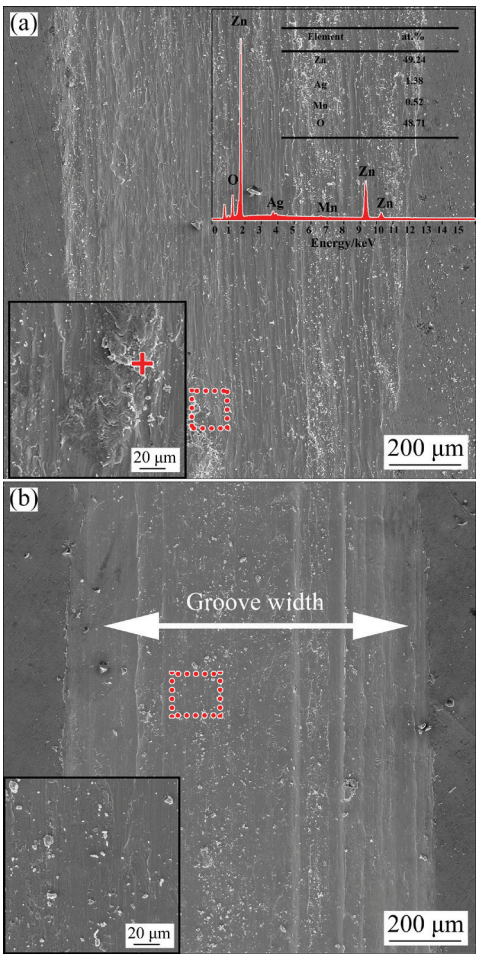


**Fig. 9** SEM morphology and EDS result of samples after wear in Hanks' solution: (a) AC Zn−4Ag−Mn; (b) HPS-treated Zn−4Ag−Mn

### 3.4 Antibacterial properties

The bacterial growth and antibacterial rate of Zn, AC Zn−4Ag−Mn and HPS-treated Zn−4Ag−Mn alloy are shown in Fig. 10. In can be seen that, Zn, AC Zn−4Ag−Mn and HPS-treated Zn−4Ag−Mn exhibited antibacterial ability, indicating both Zn and Ag ions possess certain antibacterial properties as reported [39]. However, the antimicrobial rate of 72.2% and 71.6% for AC Zn−4Ag−Mn and HPS-treated Zn−4Ag−Mn, respectively, was higher than that of pure Zn (61.1%),

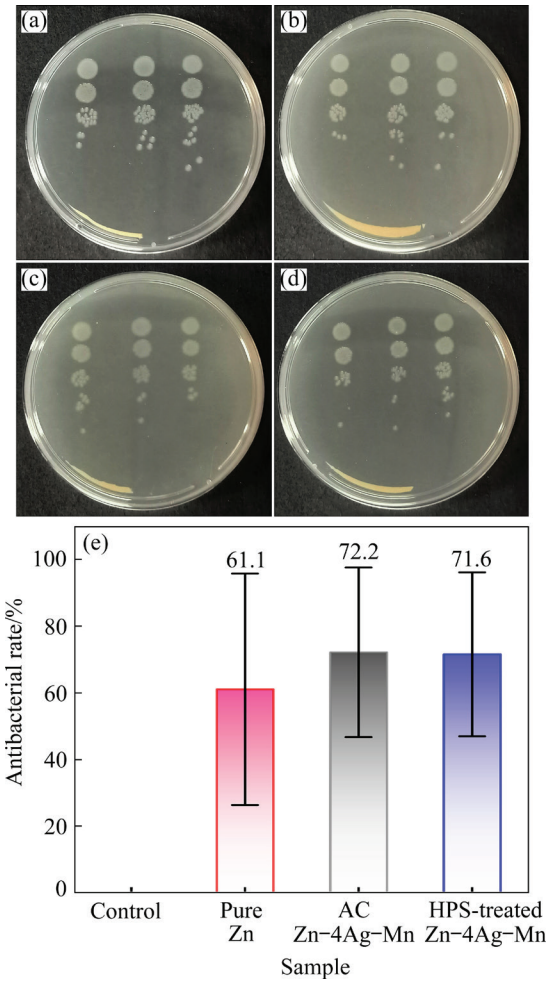


**Fig. 10** Digital photographs of bacterial growth (a−d) and antibacterial rate (e) of *E. coli* on counting plates: (a) Control; (b) Pure Zn; (c) AC Zn−4Ag−Mn; (d) HPS-treated Zn−4Ag−Mn

which illustrated that both the addition of Ag and the higher degradation rate of Zn−Ag−Mn alloy result in stronger antibacterial rate. It is reported that Ag ions released from Ag-containing materials can strongly damage the cell membranes of bacteria, thereby inhibiting the reproduction of bacteria [40−42]. What is more, Ag ions can strongly attract the hydrophobic groups of enzyme proteins in bacteria, causing the enzymes to enter an inactive state, which leads to bacterial death [43]. As HPS-treated Zn−4Ag−Mn alloy releases fewer ions than AC Zn−4Ag−Mn due to different corrosion resistances, HPS-treated alloy shows lower antibacterial rate than AC alloy.

## 4 Conclusions

(1) Both AC and HPS-treated alloys contained Zn, $AgZn_3$ and $MnZn_{13}$ phases. In HPS-treated alloy, $AgZn_3$ phases were dissolved, but fine $MnZn_{13}$ phases precipitated uniformly. The average sizes of grain and second phases were reduced to 141.67 and 10.2 μm after HPS treatment.

(2) High-pressure solid solution significantly improved the mechanical properties of Zn−4Ag−Mn alloy. The compressive yield strength and Vickers hardness of HPS alloy increased to 333.5 MPa and Hv 89.5.

(3) The high-pressure solid solution treatment improved the corrosion resistance of Zn−4Ag−Mn alloy, resulting in homogenous corrosion. The corrosion potential ($\varphi_{corr}$), corrosion current density ($J_{corr}$) and corrosion rate of HPS-treated alloy were (−1.05±0.02) V, (4.84±0.30) μA/cm$^2$ and (0.15±0.01) mm/a, respectively.

(4) The high-pressure solid solution treatment improved the wear resistance of Zn−4Ag−Mn alloy. The friction coefficients of HPS-treated and AC alloys were 0.2 and 0.35, and the wear loss were 0.2 and 0.31 mg, respectively.

(5) Zn−4Ag−Mn alloy exhibited a higher antibacterial rate than pure Zn. The antibacterial rates of pure Zn and HPS-treated Zn−4Ag−Mn were 61.1% and 71.6%, respectively.

### CRediT authorship contribution statement

**Kun-ning NIU:** Data curation, Writing − Original draft; **De-chuang ZHANG:** Conceptualization, Supervision; **Fu-gang QI:** Formal analysis, Investigation; **Jian-guo LIN:** Methodology, Funding acquisition; **Yi-long DAI:** Writing − Review & editing, Funding acquisition, Project administration.

### Declaration of competing interest

The authors declare that they have no known competing financial interests or personal relationships that could have appeared to influence the work reported in this paper.

### Acknowledgments

This study was supported by the Hunan Provincial Natural Science Foundation, China (No. 2023JJ40626), Science and Technology Innovation Program of Hunan Province, China (No. 2020RC2080), and the National Natural Science Foundation of China (No. 51971190).

### References

[1] LI Chun-mei, GUO Cheng-chen, FITZPATRICK V, IBRAHIM A, ZWIERSTRA M J, HANNA P, LECHTIG A, NAZARIAN A, LIN S J, KAPLAN D L. Design of biodegradable, implantable devices towards clinical translation [J]. Nature Reviews Materials, 2020, 5: 61−81.

[2] TSAKIRIS V, TARDEI C, CLICINSCHI F M. Biodegradable Mg alloys for orthopedic implants: A review [J]. Journal of Magnesium and Alloys, 2021, 9: 1884−1905.

[3] ZHAO Jun, JIANG Bin, SONG Yan, DAI Zuo-cai, LU Li-wei, HE Chao, HUANG Guang-sheng, ZHANG Ding-fei, PAN Fu-sheng. Simultaneous improvement of strength and ductility by Mn addition in extruded Mg−Gd−Zn alloy [J]. Transactions of Nonferrous Metals Society of China, 2022, 32: 1460−1471.

[4] YANG You-wen, YANG Ming-li, HE Chong-xian, QI Fan-wei, WANG Di, PENG Shu-ping, SHUAI Ci-jun. Rare earth improves strength and creep resistance of additively manufactured Zn implants [J]. Composites Part B: Engineering, 2021, 216: 108882.

[5] MA Xiao-chun, JIN Si-yuan, WU Rui-zhi, WANG Jia-xiu, WANG Gui-xiang, KRIT B, BETSOFEN S. Corrosion behavior of Mg−Li alloys: A review [J]. Transactions of Nonferrous Metals Society of China, 2021, 31: 3228−3254.

[6] MOSTAED E, SIKORA-JASINSKA M, DRELICH J W, VEDANI M. Zinc-based alloys for degradable vascular stent applications [J]. Acta Biomaterialia, 2018, 71: 1−23.

[7] DRYNDA A, HASSEL T, BACH F. W, PEUSTER M. In vitro and in vivo corrosion properties of new iron−manganese alloys designed for cardiovascular applications [J]. Journal of Biomedical Materials Research Part B−Applied Biomaterials, 2015, 103: 649−660.

[8] QU Xin-hua, YANG Hong-tao, JIA Bo, WANG Min-qi, YUE Bing, ZHENG Yu-feng, DAI Ke-rong. Zinc alloy-based bone internal fixation screw with antibacterial and anti-osteolytic properties [J]. Bioactive Materials, 2021, 6: 4607−4624.

[9] ZHANG Bin-bin, ZHENG Yu-feng, LIU Yang. Effect of Ag on the corrosion behavior of Ti−Ag alloys in artificial saliva solutions [J]. Dental Materials, 2009, 25: 672−677.

[10] BABA K, HATADA R, FLEGE S, ENSINGER W, SHIBATA Y, NAKASHIMA J, SAWASE T, MORIMURA T. Preparation and antibacterial properties of Ag-containing diamond-like carbon films prepared by a combination of magnetron sputtering and plasma source ion implantation [J]. Vacuum, 2013, 89: 179−184.

[11] LIU Zhi-lin, QIU Dong, WANG Feng, TAYLOR J A, ZHANG Ming-xing. The grain refining mechanism of cast zinc through silver inoculation [J]. Acta Biomaterialia, 2014, 79: 315−326.

[12] SUN Shi-neng, REN Yu-ping, WANG Li-qing, YANG Bo, LI Hong-xiao, QIN Gao-wu. Abnormal effect of Mn addition on the mechanical properties of as-extruded Zn alloys [J]. Materials Science and Engineering A, 2017, 701: 129−133.

[13] TORRES P M, VIEIRA S I, CERQUEIRA A R, PINA S, da CRUZ SILVA O A, ABRANTES J C, FERREIRA J M. Effects of Mn-doping on the structure and biological properties of beta-tricalcium phosphate [J]. Journal of Inorganic Biochemistry, 2014, 136: 57−66.

[14] GE Bing-cheng, FU Hui, DENG Kun-kun, ZHANG Qing-rui, PENG Qiu-ming. Unique strengthening mechanisms of ultrahigh pressure Mg alloys [J]. Bioactive Materials, 2018, 3: 250−254.

[15] TONG Xian, CAI Wen-hao, LIN Ji-xing, WANG Kun, JIN Lu-fan, SHI Zi-mu, ZHANG De-chuang, LIN Jian-guo, LI Yun-cang, DARGUSCH M, WEN Cui-e. Biodegradable Zn−3Mg−0.7$Mg_2Si$ composite fabricated by high-pressure solidification for bone implant applications [J]. Acta Biomaterialia, 2021, 123: 407−417.

[16] LI Wan-ying, DAI Yi-long, ZHANG De-chuang, LIN Jian-guo. Effects of ultra-high pressure solution treatment on microstructure and mechanical property of Zn−Li alloy [J]. Materials Letters, 2023, 333: 133612.

[17] LI Wan-ying, DAI Yi-long, ZHANG De-chuang, LIN Jian-guo. Biodegradable Zn–0.5Li alloys with supersaturated solid solution−aging treatment for implant applications [J]. Journal of Materials Research and Technology, 2023, 24: 9292−9305.

[18] ASTM-G102—89. Practice for calculation of corrosion rates and related information from electrochemical measurements [S].

[19] ASTM G31—72. Standard practice for laboratory immersion corrosion testing of metals [S].

[20] MA Zheng, REN Ling, LIU Rui, YANG Ke, ZHANG Yu, LIAO Zhen-hua, LIU Wei-qiang, QI Min, MISRA R D K. Effect of heat treatment on Cu distribution, antibacterial performance and cytotoxicity of Ti−6Al−4V−5Cu alloy [J]. Journal of Materials Science and Technology, 2015, 31: 723−732.

[21] SHI Zhang-zhi, YU Jing, LIU Xue-feng. Microalloyed Zn−Mn alloys: From extremely brittle to extraordinarily ductile at room temperature [J]. Materials & Design, 2018, 144: 343−352.

[22] SHI Zhang-Zhi, YU Jing, LIU Xue-feng, ZHANG Hai-jun, ZHANG Da-wei, YIN Yu-xia, WANG Lu-ning. Effects of Ag, Cu or Ca addition on microstructure and comprehensive properties of biodegradable Zn−0.8Mn alloy [J]. Materials Science and Engineering C, 2019, 99: 969−978.

[23] JIA Bo, YANG Hong-tao, HAN Yu, ZHANG Ze-chuan, QU Xin-hua, ZHUANG Yi-fu, WU Qiang, ZHENG Yu-feng, DAI Ke-rong. In vitro and in vivo studies of Zn−Mn biodegradable metals designed for orthopedic applications [J]. Acta Biomaterialia, 2020, 108: 358−372.

[24] SHUAI Ci-jun, XUE Lian-feng, GAO Cheng-de, YANG You-wen, PENG Shu-ping, ZHANG Yan-ru. Selective laser melting of Zn−Ag alloys for bone repair: Microstructure, mechanical properties and degradation behaviour [J]. Virtual and Physical Prototyping, 2018, 13: 146−154.

[25] CHEN Chun, YUE Rui, ZHANG Jian, HUANG Hua, NIU Jia-lin, YUAN Guang-yin. Biodegradable Zn−1.5Cu−1.5Ag alloy with anti-aging ability and strain hardening behavior for cardiovascular stents [J]. Materials Science and Engineering C, 2020, 116: 111172.

[26] SHI Zhang-zhi, GAO Xi-xian, ZHANG Hai-jun, LIU Xue-feng, LI Hui-yan, ZHOU Chao, YIN Yu-xia, WANG Lu-Ning. Design biodegradable Zn alloys: Second phases and their significant influences on alloy properties [J]. Bioactive Materials, 2020, 5: 210−218.

[27] GUO Kun-yu, XU Chang, LIN Xiao-ping, YE Jie, ZHANG Chong, HUANG Duo. Microstructure and strengthening mechanism of Mg−5.88Zn−0.53Cu−0.16Zr alloy solidified under high pressure [J]. Transactions of Nonferrous Metals Society of China, 2020, 30: 99−109.

[28] QU Ying-dong, LI Rong-de, YUAN Xiao-guang, LI Chen-xi, XIANG Qing-chun. New advance of alloy solidification process under high pressure [J]. Foundry, 2005, 54: 539−541. (in Chinese)

[29] WU Jia-wei, TANG Xun-hui, ZHANG Xin-ming, CEN Xi, GUO Bai-song, CHEN Biao, LI Wei, ZHANG Zhi-guo. Realizing the combination of high strength and good ductility of Cu matrix composites with CrCoNi reinforcement particles and microlaminated structure [J]. Journal of Alloys and Compounds, 2021, 872: 159632.

[30] WĄTROBA M, MECH K, BEDNARCZYK W, KAWAŁKO J, MARCISZKO-WIĄCKOWSKA M, MARZEC M, SHEPHERD D E T, BAŁA P. Long-term in vitro corrosion behavior of Zn−3Ag and Zn−3Ag−0.5Mg alloys considered for biodegradable implant applications [J]. Materials & Design, 2022, 213: 110289.

[31] SIKORA-JASINSKA M, MOSTAED E, MOSTAED A, BEANLAND R, MANTOVANI D, VEDANI M. Fabrication, mechanical properties and in vitro degradation behavior of newly developed Zn−Ag alloys for degradable implant applications [J]. Materials Science and Engineering C, 2017, 77: 1170−1181.

[32] GONG Hai-bo, WANG Kun, STRICH R, ZHOU J G. In vitro biodegradation behavior, mechanical properties, and cytotoxicity of biodegradable Zn−Mg alloy [J]. Journal of Biomedical Materials Research Part B−Applied Biomaterials, 2015, 103: 1632−1640.

[33] KUBASEK J, VOJTECH D, JABLONSKA E, POSPISILOVA I, LIPOV J, RUML T. Structure, mechanical characteristics and in vitro degradation, cytotoxicity, genotoxicity and mutagenicity of novel biodegradable Zn−Mg alloys [J]. Materials Science and Engineering C, 2016, 58: 24−35.

[34] VOLOVITCH P, ALLELY C, OGLE K. Understanding corrosion via corrosion product characterization: I. Case

study of the role of Mg alloying in Zn−Mg coating on steel [J]. Corrosion Science, 2009, 51: 1251−1262.
[35] ZENG Rong-Chang, LI Xiao-Ting, LIU Li-Jun, LI Shuo-Qi, ZHANG Fen. In vitro degradation of pure Mg for esophageal stent in artificial saliva [J]. Journal of Materials Science and Technology, 2016, 32: 437−444.
[36] BOWEN P K, DRELICH J, GOLDMAN J. Magnesium in the murine artery: probing the products of corrosion [J]. Acta Biomaterialia, 2014, 10: 1475−1483.
[37] ESHAGHI A, GHASEMI H. M, RASSIZADEHGHANI J. Effect of heat treatment on microstructure and wear behavior of Al−Si alloys with various iron contents [J]. Materials & Design, 2011, 32: 1520−1525.
[38] TONG Xian, WANG Hong-ning, ZHU Li, HAN Yue, WANG Kun, LI Yun-cang, MA Jian-feng, LIN Ji-xing, WEN Cui-e, HUANG Sheng-bin. A biodegradable in situ Zn−Mg2Ge composite for bone-implant applications [J]. Acta Biomaterialia, 2022, 146: 478−494.
[39] XIE Yu, ZHAO Li-chen, ZHANG Zhe, WANG Xin, WANG Ru, CUI Chun-xiang. Fabrication and properties of porous Zn−Ag alloy scaffolds as biodegradable materials [J]. Materials Chemistry and Physics, 2018, 219: 433−443.
[40] SONDI I, SALOPEK-SONDI B. Silver nanoparticles as antimicrobial agent: a case study on E. coli as a model for Gram-negative bacteria [J]. Journal of Colloid and Interface Science, 2004, 275: 177−182.
[41] LIAO Kuo-hsing, OU Keng-liang, CHENG Hsin-chung, LIN Che-tong, PENG Pei-wen. Effect of silver on antibacterial properties of stainless steel [J]. Applied Surface Science, 2010, 256: 3642−3646.
[42] NIU Kun-ning, ZHANG De-chuang, QI Fu-gang, LIN Jian-guo, DAI Yi-long. The effects of Cu and Mn on the microstructure, mechanical, corrosion properties and biocompatibility of Zn−4Ag alloy [J]. Journal of Materials Research and Technology, 2022, 21: 4969−4981.
[43] LI Xiao-yun, GAO Guan-hui, SUN Cheng-jun, ZHU Yao-yao, QU Ling-yun, JIANG Feng-hua, DING Hai-bing. Preparation and antibacterial performance testing of Ag nanoparticles embedded biological materials [J]. Applied Surface Science, 2015, 330: 237−244.

# 采用高压固溶制备具有均匀腐蚀行为的高强度抗菌 Zn−4Ag−Mn 合金

牛堃宁[1]，张德闯[2]，齐福刚[1]，林建国[2]，戴翌龙[1]

1. 湘潭大学 材料科学与工程学院，湘潭 411105；
2. 湘潭大学 低维材料及应用技术教育部重点实验室，湘潭 411105

**摘　要：**采用高压固溶(HPS)法制备 Zn−4Ag−Mn 合金，获得高强度、可均匀降解、抗菌的植入材料。显微组织表征表明，HPS 处理使 Zn−4Ag−Mn 合金晶粒比铸态(AC)合金的细化 57.9%，其第二相平均尺寸减小到 10.2 μm。压缩、维氏硬度和磨损摩擦试验表明，HPS 合金具有较高的力学性能，抗压屈服强度为 333.5 MPa，维氏硬度为 Hv 89.5。电化学腐蚀和浸泡腐蚀试验表明，HPS 处理优化合金的耐蚀性，使其腐蚀均匀。此外。经抗菌实验测试，HPS 处理的 Zn−4Ag−Mn 合金具有优异的抗菌性能，抗菌率为 71.6%。这些结果表明，HPS 处理的 Zn−4Ag−Mn 是一种很有前途的生物可降解植入材料。

**关键词：**Zn−Ag−Mn 合金；高压固溶；高强度；均匀腐蚀；抗菌性能

**(Edited by Bing YANG)**